ACS OMEGA

http://pubs.acs.org/journal/acsodf

Article

Gas Phase Reaction of Isocyanic Acid: Kinetics, Mechanisms, and Formation of Isopropyl Aminocarbonyl

Tien Van Pham* and Anh Van Tran

Cite This: *ACS Omega* 2021, 6, 34661−34674

Read Online

ACCESS | Metrics & More | Article Recommendations | Supporting Information

ABSTRACT: Isocyanic acid, HNCO, mainly emitted by combustion processes, is doubted to be detrimental to human health if its concentration surpasses ∼1 ppbv. Very little information has been found regarding the HNCO loss in the gas phase. This study aims to close this knowledge gap by performing a theoretical kinetic study on the reaction of HNCO with the propargyl radical. The potential energy surface of the HNCO + C_3H_3 reaction was characterized utilizing high-level CCSD(T)/CBS(TQ5)//B3LYP/6-311++G(3df,2p) quantum-chemical approaches, followed by TST and RRKM/ME kinetic computations. The obtained results reveal that the reaction can proceed via H-abstraction, leading to the C_3H_4 + NCO bimolecular products with energy barriers of 23−25 kcal/mol, and/or addition, resulting in C_4H_4NO intermediates with 23−26 kcal/mol barrier heights. The C_4H_4NO adducts when formed can decompose to products and/or return to HNCO + C_3H_3 in which the reverse decompositions are found to be dominant with a branching ratio that accounts for nearly 100% at 300 K and 760 Torr. The calculated *P*-independent rate coefficients indicate that at low temperatures, the H-abstraction channels are insignificant. However, at high temperatures ($T >$ 1500 K), the H-abstraction path leading to H_3CCCH + NCO prevails with a branching ratio of ∼50−53% in the descending 1800−1500 K temperature range at 760 Torr, while the H-abstraction leading to H_2CCCH_2 + NCO is favorable at $T >$ 1800 K, with the yield reaching above 50% at 760 Torr. In contrast to the H-abstraction rate constants, the calculated values for the additions and the C_4H_4NO decompositions show a positive pressure dependence. Both the total rate constants for the reactions HNCO + C_3H_3 → products and C_4H_4NO → products, which are, respectively, $k_{\_total\_bimo}(T) = 3.53 \times 10^{-23}T^{3.27}\exp[(-21.35 \pm 0.06\ \text{kcal/mol})/\text{RT}]$ $\text{cm}^3\ \text{molecule}^{-1}\ \text{s}^{-1}$ and $k_{\_total\_uni}(T) = 1.13 \times 10^{25}T^{-4.02}\exp[(-11.77 \pm 0.16\ \text{kcal/mol})/\text{RT}]\ \text{s}^{-1}$, increase with the increasing temperature in the 300−2000 K range at 760 Torr. The rate constant of HNCO + C_3H_3 → products is about 8 orders of magnitude smaller than the value of HCHO + C_3H_3 → products, showing that HCHO is more reactive toward the C_3H_3 free radicals than HNCO. The computed heats of formation for several species agree well with the available literature data with the deviation less than 1.0 kcal/mol, indicating that the methods used in this study are extremely reliable. With the given results, it is vigorously suggested that the predicted rate constants, together with the thermodynamic data of the species involved, can be confidently used for modeling HNCO-related systems under atmospheric and combustion conditions.

1. INTRODUCTION

Isocyanic acid (HNCO), the smallest species among the compounds containing the isocyanate functional group, evaporates easily and has moderate acidity. Although the molecular structure of isocyanic acid was first explored nearly 2 centuries ago,[1] its appearance in the atmosphere has just been identified for about 10 years.[2,3] It can bond with other substances forming H-bonded polymers which are relatively well constructed in the gas-phase environment at room temperature.[4,5] Due to the high toxicity of HNCO, it is implicated in causing adverse effects on human health (i.e., cataract, cardiovascular diseases, and rheumatoid arthritis) via a protein carbamylation process if its concentration in air exceeds 1 part per billion by volume.[2,6,7] The main source of HNCO emission into the atmosphere is from combustion processes derived from not only natural but also anthropogenic activities.[7] Particularly, Veres and co-workers[8] revealed in their experimental research that HNCO is primarily produced in the pyrolysis of nitrogen-containing biomass materials proceeding via wildfires and agricultural fires. The low-temperature coal burning process[9] and the amine and amide species photochemistry[10] can also lead to HNCO formation in the atmosphere. Moreover, HNCO is found to appear in the flue gas of gasoline and diesel engines utilizing the urea-selective catalytic reduction technique.[11,12] Urea-based additives, nicotine, and formamide available in the cigarette ingredients have been known to release HNCO through pyrolysis and/or oxidation processes.[10,13,14] Last but not least, HNCO is

Received: September 13, 2021
Accepted: November 12, 2021
Published: December 13, 2021

https://doi.org/10.1021/acsomega.1c05063

additionally emitted by burning household items (i.e., fiberglass, rubber, wood, PVC carpet, cables, and polyurethane-based foam) via surface-oxidation procedures.[7,15,16]

To our knowledge, the gas-phase chemical reaction of HNCO with other species is still limited. Only few reactions between HNCO and oxidizing agents such as OH, Cl, NO_3, and O_3 have been carefully investigated,[17−23] in which the HNCO + OH reaction was studied both experimentally (620−2500 K)[17−21] and theoretically (200−3000 K)[22,23] with the extrapolated experimental rate constant of 0.5−1.2 × 10^{-15} cm^3 $molecule^{-1}$ s^{-1} at 298 K, leading to over 25 years of lifetime of this reaction supposing a 1 × 10^6 molecule/cm^3 concentration of OH. The calculated rate constants for the HNCO + OH/Cl/NO_3/O_3 reactions,[23] $k(300\ K) \leq 0.7 \times 10^{-15}$ cm^3 $molecule^{-1}$ s^{-1}, show that all these reactions proceed slowly at ambient temperature.

In order to enrich the chemical reaction library of HNCO, in this study, we give out a comprehensive theoretical analysis of the reaction between HNCO and the propargyl radical (CH_2CCH or C_3H_3) to elucidate the mechanism and kinetics of the isopropyl aminocarbonyl (C_4H_4NO) formation and decomposition processes. The reason C_3H_3 is chosen as an oxidizing agent for the HNCO reactant is that it has been known to play a vital role in free radical chemistry, for example, it is present as a major intermediate in the flames of C_2H_2, C_4H_6, and C_6H_6, as well as in the hydrocarbon decompositions in mass spectrometry.[24−26] C_3H_3 is also known as the most dominant precursor in forming not only cyclic aromatic hydrocarbons but also soot particles and participates in the chemical transformation of N-, C-, and S-containing air pollutants into eco-friendly products.[26] Due to the high reactive ability of C_3H_3, it can interact with various species under gas-phase conditions as shown in many previously published works.[27−30] Therefore, it is impossible not to consider the possibility of the reaction between C_3H_3 and HNCO since they both appear as intermediate products in combustion processes.

Because of the current scarcity of information concerning the HNCO + C_3H_3 addition/abstraction, a crucial system in atmospheric and combustion chemistry, as well as the dissociation of the C_4H_4NO radicals, a comprehensive investigation of the mechanism and kinetics of the C_4H_4NO formation and decomposition reactions is desired and needed. The major purpose of the present work is therefore to map out the potential energy surface (PES) for the HNCO + C_3H_3 reaction utilizing a high-level density functional and ab initio quantum-chemical computations and to employ the PES data in the TST and RRKM/ME calculations of T- and P-dependent rate coefficients and product branching ratios.

2. COMPUTATIONAL METHODS

The PES of the HNCO + C_3H_3 system has been characterized using the hybrid density functional B3LYP[31−33] accompanied by the dp-polarized plus diffuse functions 6-311++G(3df,2p)[34] basis set. The B3LYP/6-311++G(3df,2p) level was also utilized to evaluate vibrational frequencies and zero-point vibrational energy corrections. In order to identify the characteristics of all species involved, their vibrational frequencies were elaborately analyzed, that is, the reactants, intermediate states, and products must hold all positive frequencies while each transition state (TS) possesses not only positive frequencies but also a negative frequency. Moreover, to confirm the right connection of TS with the preceding and following stationary points (e.g., reactants and products) through the corresponding minimum energy path, the intrinsic reaction coordinate (IRC) approach[35,36] was carried out at the same optimization method above. Before being included in the calculations for the thermodynamic parameters, the computed B3LYP/6-311++G(3df,2p) vibrational modes were scaled with a factor of 0.971 as used in a variety of previous research studies.[37−43]

The B3LYP/6-311++G(3df,2p) energies of all stationary points on the PES were then refined at the high computational cost method CCSD(T) (coupled cluster considering single, double, and perturbative triple excitations)[44] together with the aug-cc-pVTZ, aug-cc-pVQZ, and aug-cc-pV5Z basis sets,[45−47] followed by the extrapolation of the CCSD(T)/aug-cc-pVnZ (n = 3−5) single-point energies to the desired values at the complete basis set (CBS) limit. The extrapolation scheme for the CBS limit can be found in our previous work.[48] The CCSD(T)/CBS(T,Q,5) level of theory has been acknowledged as one of the most accurate protocols (e.g., the maximum absolute deviation and root-mean-square deviation do not exceed 0.28 and 0.09 kcal/mol, respectively, for test cases)[49] that was considered to be extremely appropriate for kinetic prediction in previous investigations.[50,51] To check the multi-reference character of the wavefunctions for all species involved in the HNCO + C_3H_3 system, T1 diagnostic tests[52,53] were implemented at the CCSD(T)/aug-cc-pVTZ level relied on the B3LYP/6-311++G(3df,2p) geometric structures. All the quantum-chemical computations in this system have been calculated by means of the Gaussian 16 software package.[54]

To figure out rate coefficients for the title system, the canonical TS theory (TST)[55,56] and microcanonical Rice−Ramsperger−Kassel−Marcus (RRKM) theory[57−59] have been applied with the support of the ChemRate code[60] and the Mesmer open-source programme,[61] respectively. The tunneling effect[62] was included in the kinetic treatments for the reaction paths involving in H-transfer by using a one-dimensional the asymmetrical Eckart potential. Parameters needed for calculating the density of states and the sum of states including activation barriers of the considered reaction channels on the PES, moments of inertia, and vibrational frequencies of species involved were provided as required by the Stein−Rabinovitch version of the Beyer−Swinehart algorithm.[63,64] Some kinds of single bonds (i.e., C−C, C−N, and C−O) holding low-frequency vibrational modes were handled as hindered internal rotors whose $V(\theta)$ hindrance potentials were absolutely extracted by scanning dihedral angles containing single bonds with an increasing step size of 10°, as shown in Figure S1 of the Supporting Information. In this work, Ar with the L-J parameters (ε/k_B = 113.50 K; σ = 3.465 Å)[65] was appended as the bath gas, and thus the $\langle \Delta E \rangle_{down} = 75 \times (T/300)^{1.05}$ cm^{-1} energy-transfer exponential down model[66] was applied for the kinetic model. Meanwhile, the L-J numbers for the C_4H_4NO species (σ = 6.25 Å, ε/k_B = 343 K)[65] were approximated by the values of C_6H_{14}. The unimolecular and bimolecular rate coefficients have been calculated in the 300−2000 K temperature interval in conjunction with various pressures ranging from 7.6 to 760,000 Torr using the calculated CCSD(T)/CBS(T,Q,5)//B3LYP/6-311++G(3df,2p) energy values.

3. RESULTS AND DISCUSSION

3.1. PES and Reaction Mechanism.

In order to elucidate the reaction mechanism of the HNCO + C_3H_3 system, the PES

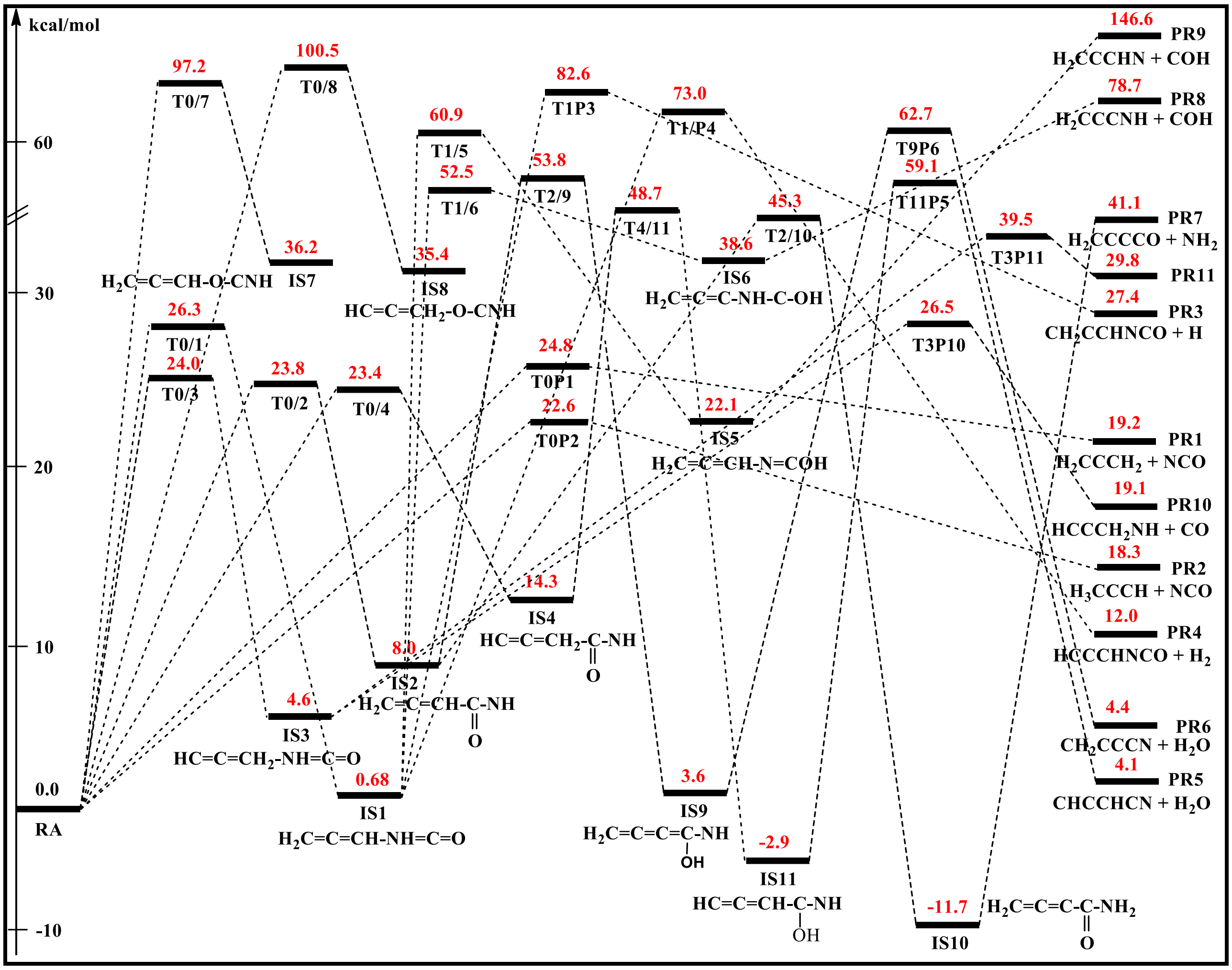

Figure 1. Detailed PES of the HNCO + C_3H_3 system calculated at the CCSD(T,Q,5)/CBS//B3LYP/6-311++G(3df,2p) + ZPEs level of theory (energies are in kcal/mol).

for this system (Figure 1) has been fully characterized by the quantum-chemical methodologies at the CCSD(T)/CBS(T,Q,5)//B3LYP/6-311++G(3df,2p) level of theory. The possible reaction paths for the formation and decomposition of C_4H_4NO are illustrated in Scheme S1 of the Supporting Information. Geometric structures of the stationary points including reactants, intermediates, and products optimized by the B3LYP/6-311++G(3df,2p) approach are displayed in Figure S2, while those of TSs are geometrically drawn in Figure S3.

Theoretical prediction of relative energies Δ*E* (kcal/mol) for reactants, intermediates, TSs, and products of the title reaction in different levels of theory has been documented in Table S1 of the Supporting Information. However, a comparison of calculated heat of formation (ΔH_{298K}) of all species in the HNCO + C_3H_3 system with available experimental data is tabulated in Table 1. Also in the Supporting Information, Table S2 exhibits Gibbs free energies (ΔG_{298K}, kcal/mol) and entropies (ΔS_{298K}, cal/mol/K) for various reaction channels calculated at the CCSD(T)/CBS(T,Q,5)//B3LYP/6-311++G(3df,2p) level of theory. Table S3 presents the harmonic vibrational frequencies of all species involved on the PES, while their reaction coordinates in the Cartesian form are available in Table S4. In this study, the geometries of several major TSs have also been optimized by two other methods, namely, M062X and MP2(full), and their single-point energies have been absolutely refined at the CCSD(T)/CBS(T,Q,5) level; both the methods give almost the same values and they are not far from the CCSD(T)/CBS(T,Q,5)//B3LYP/6-311++G(3df,2p) values shown in Table S5 of the Supporting Information.

In order to probe the multireference character of the used wavefunction, the T1 diagnostic values of the open-shell stationary points have been computed at the restricted coupled-cluster RCCSD(T)/aug-cc-pVTZ level, while those of the closed-shell species have been predicted at the unrestricted coupled-cluster UCCSD(T)/aug-cc-pVTZ level. The calculated T1 diagnostics results for the reactants, intermediate states, TSs, and products of the title reaction are tabulated in Table S6 of the Supporting Information. As can be seen, the T1 diagnostics of nearly all closed-shell species for the present study are less than 0.02 except for only one value of 0.025 which belongs to H_2CCCHN (PR9), while those of almost open-shell species are in the range of 0.01−0.044 except for three values of 0.055, 0.046, and 0.053 corresponding to T0/7, T2/10, and H_2CCCCN (PR6), respectively. However, the four species (T0/7, T2/10, PR6, and PR9) can be ignored when exploring the C_4H_4NO system due to their disadvantage in energy as discussed below. Hence, the single-reference methods can be reliably employed in this

Table 1. Comparison of Heats of Formation (at 298 K, in kcal/mol) of All Structures Related to the Title Reaction[a] with Literature Data[b]

species	ΔH_{298K}	species	ΔH_{298K}
C_3H_3 (propargyl radical)	83.56 (84.02 ± 0.39[b])	T0P1	24.05
HNCO (isocyanic acid)	−29.12 (−28.45 ± 0.37[b])	T0P2	21.79
IS1	−0.45	T1/5	59.72
IS2	6.82	T1/6	51.19
IS3	3.57	T1P3	81.70
IS4	12.33	T1P4	71.68
IS5	21.09	T11P5	58.19
IS6	37.81	T2/10	44.29
IS7	35.25	T2/9	52.45
IS8	34.37	T4/11	47.30
IS9	2.69	T9P6	62.01
IS0	−12.30	H_2CCCH_2	45.02 (45.43 ± 0.32[b])
IS11	−4.14	$HCCCH_3$	43.52 (44.38 ± 0.32[b])
T0/1	25.53	NCO	30.83 (30.44 ± 0.38[b])
T0/2	22.89	H_2O	−60.15 (−57.80 ± 0.03[b])
T0/3	23.22	NH_2	44.33 (44.47 ± 0.15[b])
T0/4	22.39	COH	−25.67 (−26.42 ± 0.03[b])
T0/7	96.43	CO	51.78 (52.10 ± 0.70[b])
T0/8	99.70		

[a]This work calculated at the CCSD(T)/CBS(T,Q,5)//B3LYP/6-311++G(3df,2p) level of theory. [b]Values collected from active thermochemical tables (ATcT).[67,68]

work. In addition, the table also reveals that the spin contamination numbers for all doublet-state species do not exceed 0.78, while those for singlet-state species get a zero value, showing that the spin contamination influences on the evaluation of energy barriers and the optimization of all structures involved are insignificant.

(a) Direct H-abstraction pathways

It can be seen from the PES that there are two possibilities to expel hydrogen atom out of the HNCO molecule. The first possibility occurs when the (CH) head of the propargyl radical ($CH_2{=}C{=}CH$) attacks the HNCO hydrogen atom through the T0P1 TS, while the second one proceeds via the T0P2 saddle point when the other head of C_3H_3 strikes the HNCO hydrogen atom. If the first TS holds an energy level of 24.8 kcal/mol, the second one needs to pass over an energy barrier of 22.6 kcal/mol calculated at the CCSD(T)/CBS(T,Q,5)//B3LYP/6-311+++G(3df,2p) level of theory. Accordingly, the first direct H-abstraction channel HNCO + C_3H_3 → T0P1 → PR1 (H_2CCCH_2 + NCO) consumes about 2 kcal/mol more than the second channel HNCO + C_3H_3 → T0P2 → PR2 (H_3CCCH + NCO). These results indicate that the formation processes of the PR1 and PR2 products are considered to be competitive with each other.

In the T0P1 structure (see Figure S3), the H atom attached to the N atom separates at a bond length of 1.43 Å, and the bond between this atom and the CH group of the C_3H_3 radical is formed at a distance of 1.21 Å; these processes are characterized by an imaginary frequency of 839i cm^{-1}. In order to facilitate the formation of a new bond between the CH group and the H atom, the ∠HCC bond angle is decreased by 60° from 180° in C_3H_3 to 130° in T0P1, which suggests that this transition is a critical motion in the T0P1 TS and relates to the re-hybridization of the carbon atom from sp to sp^2. In the final product, PR1 (H_2CCCH_2 + NCO), the newly formed C−H bond length is shortened to 1.08 Å in the H_2CCCH_2 fragment. Similarly, in the structure of T0P2, the H−NCO bond is split at a 1.47 Å distance, and a new $H_2C{-}H$ bond is formed with a 1.21 Å bond length, which is then shortened to 1.09 Å in the H_3CCCH molecule of the PR2 product; a negative frequency recorded for those harmonic vibrations is 577i cm^{-1} (Table S3). Contemporarily, the ∠HCC bond angle in the T0P2 geometry reaches 110°, which is perfectly consistent with the sp^3 hybridization and the tetrahedral structure of the $-CH_3$ carbon atom in the H_3CCCH molecule. It should be mentioned that the IRC scanning results for both T0P1 and T0P2, as shown in Figure S4, have confirmed that T0P1 connects between the reactants and the PR1 product while T0P2 is the highest point on the reaction path going from the entrance point to the PR2 product.

It is easy to see that, on the other hand, reaction channels leading to the two PR1 and PR2 products have been found to be endothermic by approximately 19 and 18 kcal/mol, respectively, predicted at the CCSD(T)/CBS(T,Q,5)//B3LYP/6-311++G(3df,2p) level. On the thermodynamic side, the PR2 product produced by the second separation channel going via the C_1 symmetry TS (T0P2) is slightly stable in comparison with the PR1 product created by the first one.

(b) Addition pathways

There are six possible pathways for the X-addition on the propargyl radical, where X stands for the atoms of N, C, or O. First, the HNCO nitrogen atom can add on the CH carbon atom of $CH_2{=}C{=}CH$ via the T0/1 TS, leading to the first intermediate state, namely, IS1: $H_2C{=}C{=}CH{-}NH{=}C{=}O$, or it can attack the CH_2 carbon atom through T0/3 to form the isomer IS3: $HC{=}C{=}CH_2{-}NH{=}C{=}O$. The former pathway must overcome a barrier of 26.3 kcal/mol while the latter has a barrier of 24 kcal/mol. These CCSD(T)/CBS(T,Q,5)//B3LYP/6-311++G(3df,2p) barriers are about 1.0 kcal/mol higher than the CCSD(T)/CBS(T,Q,5)//M06-2X/aug-cc-pVTZ barriers. Although the energy level of T0/1 is higher than that of T0/3, the relative energy of IS1 formed by T0/1 is lower than that of IS3 created by T0/3 (0.68 kcal/mol vs 4.6 kcal/mol). The structure of T0/1 displayed in Figure S3 shows that a new bond distance between the propargyl radical and isocyanic acid is 1.898 Å; its harmonic vibration is identified by an imaginary frequency of ∼648i cm^{-1}. To facilitate the newly formed bond, the ∠HCC bond angle of the $HCCCH_2$ moiety has been reduced by nearly 40°, while the ∠HNC bond angle of the HNCO moiety decreased by only ∼2°. Similar to T0/1, the T0/3 geometry reveals that the loose $HCCC(H_2){-}N(H)CO$ bond holds a 1.918 Å distance whose harmonic vibration was identified by a ∼649i cm^{-1} imaginary frequency; the $\angle CCH_2$ dihedral angle of the $HCCCH_2$ fragment lost ∼38° from 180° while the ∠HNC bond angle of the HNCO species was brought down by ∼3°. Second, the HNCO carbon atom can assail on both the head and tail of the $CH_2{=}C{=}CH$ radical via the T0/2 and T0/4 saddle points, resulting in two adducts IS2 $H_2C{=}C{=}CH{-}C(O){-}NH$ and IS4 $HC{\equiv}C{-}CH_2{-}C(O){-}NH$, respectively. As can be seen in

Figure 1, these two channels must go across a similar barrier of around 23.5 kcal/mol, indicating that the IS2 and IS4 isomers have the same formation possibility. However, the IS2 intermediate when formed has only about half the energy of the IS4 value, 8 kcal/mol versus 14.3 kcal/mol, which means that the former is more stable than the latter in terms of thermodynamics. Unlike T0/1 and T0/3, in the structures of both T0/2 and T0/4 (see Figure S3), the HNCO molecule is located perpendicularly to the carbon chain of C_3H_3 when the HNCO carbon atom attacks on the head or tail of the propargyl radical. The B3LYP/6-311++G(3df,2p) geometry of T0/2 shows that the newly formed bond length C−C between C_3H_3 and HNCO is 1.839 Å, recognized by a 536i cm^{-1} imaginary frequency and the ∠NCO bond angle of the HNCO moiety reaches 145° instead of 173° while those parameters of T0/4 are documented to be 1.809 Å identified by a 556i cm^{-1} vibrational frequency and 141°, respectively. Lastly, two other intermediate states IS7 and IS8 can be generated by attacking the HNCO oxygen atom onto the CH and CH_2 carbon atoms of C_3H_3 through two TSs T0/7 and T0/8, respectively. The mechanism shown in Figure 1 reveals that these two saddle points stand at very high levels of energy relative to the reactants, 97.2 and 100.5 kcal/mol. Hence, the two adducts IS7 and IS8 are extremely difficult to be produced by the two bimolecular addition channels HNCO + C_3H_3 → IS7 (via T0/7) and HNCO + C_3H_3 → IS8 (via T0/8). Moreover, these adducts whose relative energies are known to be 36.2 and 35.4 kcal/mol are also unstable in energy as opposed to the previous isomers IS1−IS4 (0.7−14 kcal/mol). Therefore, the two reaction paths indicated above were stopped at the IS7 and IS8 locations without further consideration because they are infeasible in terms of energy, and these channels will also be not considered for kinetic calculations.

From the IS1 ($H_2C{=}C{=}CH{-}NH{=}C{=}O$) adduct, four bimolecular products PR3, PR4, PR8, and PR9 can be formed, in which the PR3 ($CH_2CCHNCO$ + H) and PR4 ($HCCCHNCO + H_2$) products are created directly via the T1P3 and T1P4 TSs, whereas the PR8 (H_2CCCNH + COH) and PR9 (H_2CCCHN + COH) products are generated indirectly through the IS5 and IS6 intermediate species. If the one-step reaction path going from IS1 via T1P3 to PR3 displays an H-abstraction process, the multi-step IS1 → T1P4 → PR4 reaction channel shows a H_2-loss procedure. In the T1P3 structure shown in Figure S3, the NH hydrogen atom is abstracting at a quite long distance of 1.616 Å, which is suitable for a TS. Only one imaginary frequency of ∼955i cm^{-1} was recognized among the harmonic oscillator frequencies of this TS. Unlike the T1P3 geometric structure, in the T1P4 framework, both hydrogen atoms are going far away from the CH_2 and NH groups at the distances of 1.333 and 1.395 Å, respectively, and distance between them is 0.985 Å, which facilitates them in combining to create a H_2 molecule. Due to such simultaneous H-abstraction processes, the imaginary frequency of T1P4 was recorded to be significantly larger than that of T1P3, which is 1577i cm^{-1}. In addition, to accelerate for the H_2 loss, the ∠CCC bond angle of the H_2CCCH moiety in the T1P4 structure is reduced by ∼53° from nearly 180° while the ∠NCO bond angle of the HNCO moiety is increased by ∼47° from about 130° (see Figure S3). Data shown in Figure 1 point out that the T1P3 energy barrier is approximately 10 kcal/mol higher than that of T1P4, indicating that the PR4 product is favored over the PR3 product. In terms of thermodynamics, the former is more stable than the latter, 12 versus 27.4 kcal/mol, and the formation of both is seen to be endothermic. It is easy to see that the two remaining products, PR8 (H_2CCCNH + COH) and PR9 (H_2CCCHN + COH), are isomers of each other. Of these products, the first one was formed by the IS1 → IS6 → PR8 channel while the second one was produced by the IS1 → IS5 → PR9 channel. Both channels are two-step reaction paths, but each contains exactly one well-defined TS (T1/5 or T1/6) where T1/6 connecting between IS1 and IS6 belongs to the former channel and T1/5 bridging between IS1 and IS5 belongs by the latter reaction path. The calculated results indicate that the T1/6 energy level is nearly 8.5 kcal/mol smaller than that of the T1/5 TS, showing that IS6 is easily formed than IS5. However, the IS6 intermediate state is unstable compared to the IS5 isomer because the IS6 relative energy is much higher than that of the IS5 species, which is 38.6 and 22.1 kcal/mol, respectively. The T1/5 structure displayed in Figure S3 discloses that the hydrogen atom is transferred from the NH group to the oxygen atom with the weak bond lengths N−H and H−O of 1.397 and 1.328 Å, respectively. To assist the H movement, the HNCO moiety is converted from a chair form to a boat form, which makes the ∠CNC and ∠NCO bond angles reach new values of 130 and 140°, respectively (Figure S3). Following the formation of IS5 and IS6, two bimolecular products PR9 (H_2CCCHN + COH) and PR8 (H_2CCCNH + COH), respectively, were directly formed without passing through any well-defined TS. The overall endothermicity of the process leading to the PR8 product is nearly 79 kcal/mol while that of the reaction channel resulting in the PR9 product is approximately 147 kcal/mol. These data reveal that both the PR8 and PR9 products are hardly formed under ambient conditions, and they are also less stable products in comparison with the others on the PES. Therefore, the reaction paths leading to these products from IS1 will not be considered for kinetic computations.

From the IS2 ($H_2C{=}C{=}CH{-}C(O){-}NH$) adduct, two bimolecular products PR6 and PR7 have been established, in which the first one was formed by the IS2 → IS9 → PR6 channel while the second one was formed by the IS2 → IS10 → PR7 reaction path. In the former channel, the IS2 intermediate state isomerizes to IS9 at the first step via a T2/9 TS whose H-shift proceeds between the CH group and the O atom with long distances of 1.304 and 1.379 Å, respectively. This transfer was determined by an imaginary frequency of 1990i cm^{-1}. The isomerization step must overcome a barrier of ∼46 kcal/mol, which is about 30 kcal/mol larger than the re-dissociation step of IS2 back to the C_3H_3 + HNCO reactants. Therefore, the decomposition of IS2 is energetically favored over the isomerization. This feature is also true for both IS1 and IS4 cases. Subsequently, IS9, with 3.6 kcal/mol available internal energy, could dissociate into the PR6 ($CH_2CCCN + H_2O$) product via the T9P6 saddle point located at nearly 63 kcal/mol above the starting point. The T9P6 structure shown in Figure S3 indicates that the NH hydrogen atom moves to the OH group before the C−O bond scission process, forming a water molecule whose relative energy sharing with a CH_2CCCN moiety is 4.4 kcal/mol. The moving bonds of N−H and O−H in the T9P6 saddle point are recorded to be 1.265 and 1.333 Å, respectively, while the C−O bond breaking reaches a distance of 1.859 Å. The energy barrier of T9P6 is so high, around 59 kcal/mol, indicating that the IS9 → PR6 dissociation channel is not energetically

Table 2. Bimolecular k_1−k_7 Rate Constants (in Units of cm^3 $molecule^{-1}$ s^{-1}) of the HNCO + C_3H_3 Reactions Calculated at T = 300−2000 K and P = 760 Torr (Ar), where k_1−k_4 Are Values of the HNCO + C_3H_3 → C_4H_4NO (IS1−IS4) Channels, while k_5/k_6 and k_7 Are the Numbers of the HNCO + C_3H_3 → H_2CCCH_2 + NCO (PR1)/$HCCCH_3$ + NCO (PR2) and HNCO + C_3H_3 → $HCCCH_2NH$ + CO (PR10) Channels

T (K)	k_1	k_2	k_3	k_4	k_5	k_6	k_7
300	3.26×10^{-33}	1.03×10^{-31}	1.91×10^{-31}	3.69×10^{-31}	4.41×10^{-32}	1.14×10^{-30}	5.89×10^{-37}
400	2.23×10^{-28}	2.47×10^{-27}	5.21×10^{-27}	6.28×10^{-27}	2.55×10^{-27}	2.59×10^{-26}	6.51×10^{-31}
500	1.80×10^{-25}	1.06×10^{-24}	2.44×10^{-24}	1.77×10^{-24}	2.03×10^{-24}	1.17×10^{-23}	2.63×10^{-27}
600	1.56×10^{-23}	5.83×10^{-23}	1.45×10^{-22}	6.66×10^{-23}	1.89×10^{-22}	7.42×10^{-22}	6.49×10^{-25}
700	3.75×10^{-22}	9.35×10^{-22}	2.57×10^{-21}	8.08×10^{-22}	5.14×10^{-21}	1.53×10^{-20}	3.25×10^{-23}
800	4.00×10^{-21}	6.68×10^{-21}	2.03×10^{-20}	4.88×10^{-21}	6.47×10^{-20}	1.56×10^{-19}	6.02×10^{-22}
900	2.45×10^{-20}	2.78×10^{-20}	9.07×10^{-20}	1.87×10^{-20}	4.85×10^{-19}	9.87×10^{-19}	5.76×10^{-21}
1000	9.99×10^{-20}	8.03×10^{-20}	2.68×10^{-19}	5.24×10^{-20}	2.52×10^{-18}	4.48×10^{-18}	3.47×10^{-20}
1100	2.96×10^{-19}	1.82×10^{-19}	5.93×10^{-19}	1.17×10^{-19}	1.03×10^{-17}	1.59×10^{-17}	1.50×10^{-19}
1200	6.80×10^{-19}	3.51×10^{-19}	1.08×10^{-18}	2.23×10^{-19}	3.25×10^{-17}	4.70×10^{-17}	5.03×10^{-19}
1300	1.27×10^{-18}	5.99×10^{-19}	1.74×10^{-18}	3.74×10^{-19}	9.01×10^{-17}	1.20×10^{-16}	1.40×10^{-18}
1400	1.99×10^{-18}	9.33×10^{-19}	2.54×10^{-18}	5.70×10^{-19}	2.20×10^{-16}	2.73×10^{-16}	3.33×10^{-18}
1500	2.83×10^{-18}	1.36×10^{-18}	3.48×10^{-18}	8.06×10^{-19}	4.84×10^{-16}	5.64×10^{-16}	7.04×10^{-18}
1600	3.71×10^{-18}	1.88×10^{-18}	4.52×10^{-18}	1.07×10^{-18}	9.80×10^{-16}	1.08×10^{-15}	1.35×10^{-17}
1700	4.62×10^{-18}	2.49×10^{-18}	5.65×10^{-18}	1.36×10^{-18}	1.85×10^{-15}	1.95×10^{-15}	2.39×10^{-17}
1800	5.54×10^{-18}	3.15×10^{-18}	6.84×10^{-18}	1.66×10^{-18}	3.29×10^{-15}	3.32×10^{-15}	3.97×10^{-17}
1900	6.46×10^{-18}	3.81×10^{-18}	8.07×10^{-18}	1.96×10^{-18}	5.56×10^{-15}	5.39×10^{-15}	6.23×10^{-17}
2000	7.38×10^{-18}	4.52×10^{-18}	9.33×10^{-18}	2.25×10^{-18}	9.00×10^{-15}	8.43×10^{-15}	9.31×10^{-17}

favorable. Similar to the IS2 → IS9 step, the IS2 → IS10 isomerization must overcome a tight T2/10 transition state with an energy barrier height of ~37 kcal/mol to form a IS10 isomer before generating to the PR7 (H_2CCCCO + NH_2) product. It should be noted that the IS10 stationary point is the most thermodynamically stable species all over the PES, and its relative energy was predicted to be nearly 12 kcal/mol under the free reactants. The B3LYP/6-311++G(3df,2p) geometry of T2/10 shows that the CH hydrogen atom is transferred to the NH group, in which the C−H bond breaking and the N−H bond formation hold respective bond lengths of 1.324 and 1.428 Å. Unlike the IS9 → PR6 step, however, the IS10 → PR7 dissociation is a barrierless process. Compared to the PR6 product, PR7 is less stable with a relative energy of 41 kcal/mol.

Following the formation of IS3, the PR10 ($HCCCH_2NH$ + CO) and PR11 ($HCCCH_2NCO$ + H) product pairs have been directly produced proceeding via the well-defined TSs T3P10 and T3P11, respectively, in which the first product is favored in comparison with the second one because the IS3 → PR10 activation barrier is much lower than that of the IS3 → PR11 dissociation, 26.5 kcal/mol versus 39.5 kcal/mol. The reaction path leading to the PR10 product is therefore considered for the kinetic calculation. If the IS3 → PR10 decomposition displays a CO-loss process, the IS3 → PR11 dissociation illustrates an H-loss procedure. Both channels are endothermic processes with energies absorbed of ~19 and ~30 kcal/mol, respectively. Far apart from IS3, IS4 can first isomerize to IS11 (HC═C═CH−C(OH)−NH, −3 kcal/mol) via T4/11 with a ~34 kcal/mol barrier height, followed by decomposition to product PR5 (CHCCHCN + H_2O) via T11P5 with a barrier of 62 kcal/mol calculated at the CCSD(T)/CBS(T,Q,5)//B3LYP/6-311++G(3df,2p) level of theory. The overall endothermicity of the reaction channel leading to the PR5 product is about 4 kcal/mol calculated at the same level mentioned above. The calculated results exhibited in Figure 1 indicate that the PR5 product is the lowest-lying bimolecular product as opposed to the others. The lower TS of the two, known as T4/11, however, still lies 49 kcal/mol above the entry point. Hence, the IS4 intermediate state will preferentially convert to the initial reactants instead of generating the PR5 product as mentioned above.

From the above-analyzed data, it can be concluded that among 11 bimolecular products of the title system, only three products (PR1, PR2, and PR10) can be formed under normal conditions, all the others are mainly controlled by the extremely high TSs and are therefore expected to be thermodynamically and kinetically unfavorable. The results given above have also clearly demonstrated that the H-abstraction processes are strongly competitive with the addition reactions. The rate constant computations in the subsequent main section allow us to confirm these conclusions.

3.2. Thermochemical Properties. To assess the accuracy of such calculations, the calculated thermodynamic property (ΔH_{298K}) for all species involved in the HNCO + C_3H_3 system is presented in Table 1 and compared to the literature data of several limited species (e.g., C_3H_3, HNCO, H_2CCCH_2, $HCCCH_3$, NCO, H_2O, NH_2, COH, and CO). As shown in Table 1, the predicted values are well consistent with the literature values within their uncertainties, for example, the maximum deviation between our values and ATcT is less than 1.0 kcal/mol. Such good agreements on the calculated thermodynamic parameter reveal that the selected method is a reasonably suitable choice for the title reaction.

4. RATE CONSTANTS AND PRODUCT BRANCHING RATIOS

Rate coefficients of the HNCO + C_3H_3 bimolecular reaction and the C_4H_4NO unimolecular decomposition have been calculated based on the CCSD(T)/CBS(T,Q,5)//B3LYP/6-311++G(3df,2p) + ZPEs PES. As stated above, the HNCO + C_3H_3 → IS7/IS8 addition reactions and the C_4H_4NO (IS1−IS4) → (PR3−PR11) decomposition reactions can be ignored because they must overcome the high activation barriers except for the IS3 → PR10 channel holding the low-energy TS (Figure 1). Therefore, the first-order and second-order rate

Table 3. Unimolecular k_{-1}−k_{-5} Rate Constants (in Units of s^{-1}) of the C_4H_4NO (IS1−IS4) → HNCO + C_3H_3 and C_4H_4NO (IS3) → $HCCCH_2NH$ + CO (PR10) Decomposition Reactions Calculated at T = 300−2000 K and P = 760 Torr (Ar)

T (K)	k_{-1}	k_{-2}	k_{-3}	k_{-4}	k_{-5}
300	5.24×10^{-6}	3.98×10^{1}	1.22×10^{-1}	2.96×10^{6}	1.92×10^{-3}
400	3.40×10^{-1}	4.20×10^{4}	5.85×10^{2}	1.54×10^{8}	2.47×10^{1}
500	2.61×10^{2}	2.66×10^{6}	9.39×10^{4}	1.25×10^{9}	6.99×10^{3}
600	2.12×10^{4}	3.88×10^{7}	2.65×10^{6}	4.17×10^{9}	2.84×10^{5}
700	4.71×10^{5}	2.31×10^{8}	2.65×10^{7}	8.65×10^{9}	3.67×10^{6}
800	4.60×10^{6}	7.58×10^{8}	1.33×10^{8}	1.35×10^{10}	2.20×10^{7}
900	2.56×10^{7}	1.67×10^{9}	4.05×10^{8}	1.78×10^{10}	7.62×10^{7}
1000	9.48×10^{7}	2.83×10^{9}	8.64×10^{8}	2.08×10^{10}	1.75×10^{8}
1100	2.56×10^{8}	4.09×10^{9}	1.45×10^{9}	2.24×10^{10}	3.02×10^{8}
1200	5.39×10^{8}	5.35×10^{9}	2.08×10^{9}	2.29×10^{10}	4.25×10^{8}
1300	9.28×10^{8}	6.55×10^{9}	2.70×10^{9}	2.25×10^{10}	5.26×10^{8}
1400	1.36×10^{9}	7.68×10^{9}	3.30×10^{9}	2.15×10^{10}	5.97×10^{8}
1500	1.82×10^{9}	8.71×10^{9}	3.85×10^{9}	2.02×10^{10}	6.34×10^{8}
1600	2.25×10^{9}	9.65×10^{9}	4.35×10^{9}	1.86×10^{10}	6.41×10^{8}
1700	2.66×10^{9}	1.05×10^{10}	4.79×10^{9}	1.70×10^{10}	6.25×10^{8}
1800	3.05×10^{9}	1.11×10^{10}	5.18×10^{9}	1.54×10^{10}	5.92×10^{8}
1900	3.41×10^{9}	1.15×10^{10}	5.52×10^{9}	1.39×10^{10}	5.49×10^{8}
2000	3.74×10^{9}	1.18×10^{10}	5.82×10^{9}	1.24×10^{10}	4.99×10^{8}

coefficients of the C_4H_4NO decomposition and the HNCO + C_3H_3 addition/abstraction, respectively, were computed based on the reaction channels presented as follows.

$$\mathrm{HNCO} + \mathrm{C_3H_3} \rightarrow \mathrm{IS1\ via\ T0/1} \tag{k1}$$

$$\mathrm{HNCO} + \mathrm{C_3H_3} \rightarrow \mathrm{IS2\ via\ T0/2} \tag{k2}$$

$$\mathrm{HNCO} + \mathrm{C_3H_3} \rightarrow \mathrm{IS3\ via\ T0/3} \tag{k3}$$

$$\mathrm{HNCO} + \mathrm{C_3H_3} \rightarrow \mathrm{IS4\ via\ T0/4} \tag{k4}$$

$$\mathrm{HNCO} + \mathrm{C_3H_3} \rightarrow \mathrm{H_2CCCH_2} + \mathrm{NCO\ via\ T0P1} \tag{k5}$$

$$\mathrm{HNCO} + \mathrm{C_3H_3} \rightarrow \mathrm{HCCCH_3} + \mathrm{NCO\ via\ T0P2} \tag{k6}$$

$$\mathrm{HNCO} + \mathrm{C_3H_3} \rightarrow \mathrm{HCCCH_2NH} + \mathrm{CO\ via\ T0/3\ and\ T3P10} \tag{k7}$$

$$\mathrm{IS}\vec{1} \rightarrow \mathrm{HNCO} + \mathrm{C_3H_3}\ \mathrm{via\ T0/1} \tag{k-1}$$

$$\mathrm{IS}\vec{2} \rightarrow \mathrm{HNCO} + \mathrm{C_3H_3}\ \mathrm{via\ T0/2} \tag{k-2}$$

$$\mathrm{IS}\vec{3} \rightarrow \mathrm{HNCO} + \mathrm{C_3H_3}\ \mathrm{via\ T0/3} \tag{k-3}$$

$$\mathrm{IS}\vec{4} \rightarrow \mathrm{HNCO} + \mathrm{C_3H_3}\ \mathrm{via\ T0/4} \tag{k-4}$$

$$\mathrm{IS}\vec{3} \rightarrow \mathrm{HCCCH_2NH} + \mathrm{CO\ via\ T3P10} \tag{k-5}$$

The bimolecular rate constants of the HNCO + C_3H_3 addition/abstraction reactions (k_1−k_6) have been computed by the TST approach, while the unimolecular rate coefficients of the C_4H_4NO → (HNCO + C_3H_3)/($HCCCH_2NH$ + CO) decomposition reactions (k_{-1}−k_{-5}) and the HNCO + C_3H_3 → $HCCCH_2NH$ + CO bimolecular rate coefficient (k_7) have been predicted by the RRKM theory. The MESMER code was used for the k_1−k_4, k_7, and k_{-1}−k_{-5} rate-coefficient predictions, whereas the ChemRate software package was utilized for the k_5 and k_6 computations.

The second-order k_1−k_6 rate constants in the 300−2000 K temperature range and at 760 Torr (Ar) pressure for the processes HNCO + C_3H_3 → C_4H_4NO (IS1−IS4) and HNCO + C_3H_3 → H_2CCCH_2 + NCO (PR1)/$HCCCH_3$ + NCO (PR2) as well as HNCO + C_3H_3 → $HCCCH_2NH$ + CO (PR10) are shown in Table 2, whereas the first-order k_{-1}−k_{-5} rate coefficients under the same conditions for the C_4H_4NO (IS1−IS4) → C_3H_3 + HNCO and C_4H_4NO (IS3) → $HCCCH_2NH$ + CO (PR10) channels are tabulated in Table 3. The values of k_1−k_7 and k_{-1}−k_{-5} over the 300−2000 K and 7.6−76,000 Torr ranges are presented in Tables S7−S14 in the Supporting Information. The plots of the temperature- and pressure-dependent rate constants and the branching ratios for the channels indicated are graphically displayed in Figures 2−15.

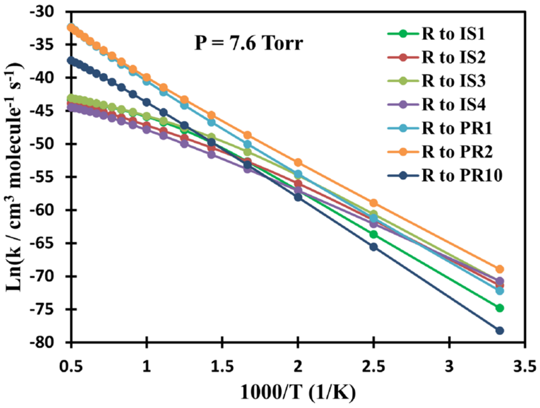

Figure 2. Plots of the predicted individual rate constants of the HNCO + C_3H_3 (R) reaction forming the C_4H_4NO (IS1−IS4) adducts and/or the H_2CCCH_2 + NCO (PR1)/$HCCCH_3$ + NCO (PR2) products in the 300−2000 K range and 7.6 Torr (Ar).

Overall, as can be seen from Figures 2−6, the bimolecular pressure-dependent rate constants (k_1−k_4, k_7) of the HNCO + C_3H_3 system tend to increase rapidly with rising temperatures in the given range. It is worth noting that while the k_1−k_4 temperature-dependent rate constants show an increasing tendency when pressure goes up, covering the considered P-range, the k_7 value displays an opposite trend. Unlike the k_1−k_4 and k_7 values, both the k_5 and k_6 temperature-dependent values

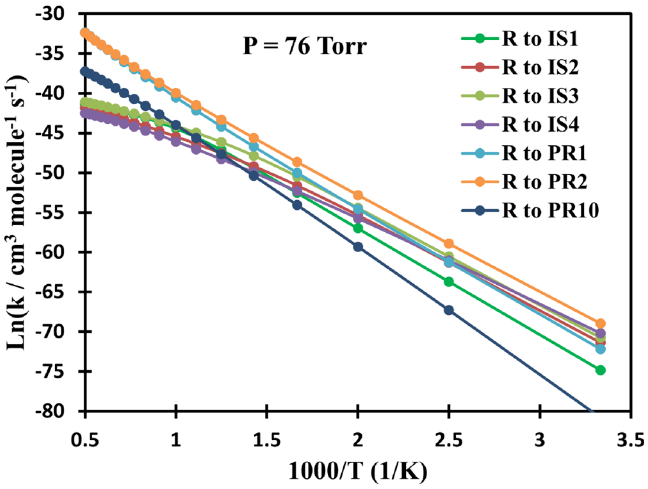

Figure 3. Plots of the predicted individual rate constants of the HNCO + C_3H_3 (R) reaction forming the C_4H_4NO (IS1–IS4) adducts and/or the H_2CCCH_2 + NCO (PR1)/$HCCCH_3$ + NCO (PR2) products in the 300–2000 K range and 76 Torr (Ar).

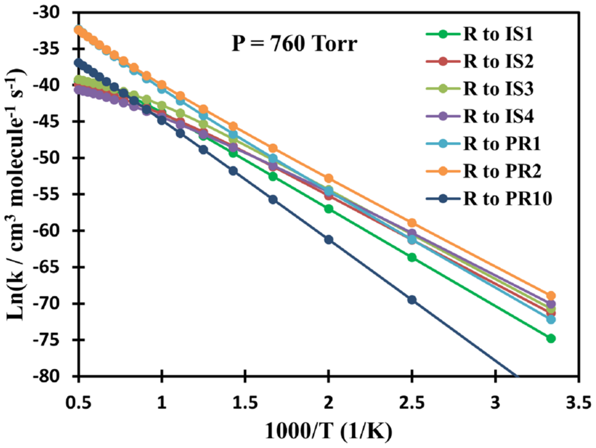

Figure 4. Plots of the predicted individual rate constants of the HNCO + C_3H_3 (R) reaction forming the C_4H_4NO (IS1–IS4) adducts and/or the H_2CCCH_2 + NCO (PR1)/$HCCCH_3$ + NCO (PR2) products in the 300–2000 K range and 760 Torr (Ar).

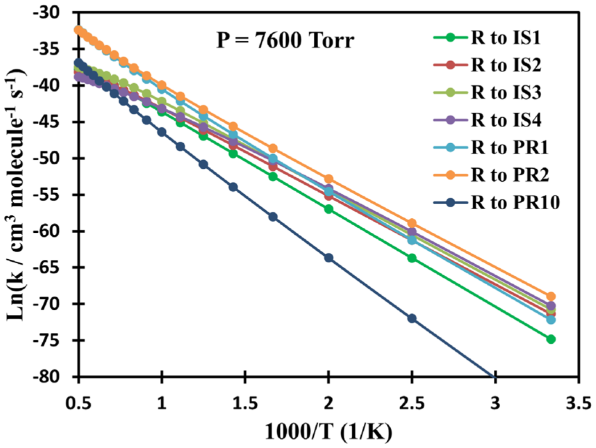

Figure 5. Plots of the predicted individual rate constants of the HNCO + C_3H_3 (R) reaction forming the C_4H_4NO (IS1–IS4) adducts and/or the H_2CCCH_2 + NCO (PR1)/$HCCCH_3$ + NCO (PR2) products in the 300–2000 K range and 7600 Torr (Ar).

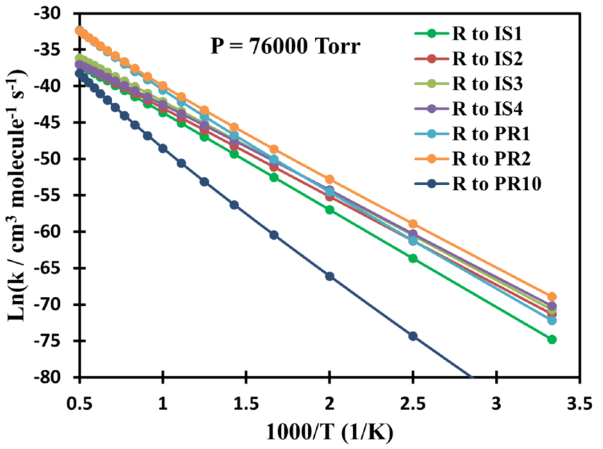

Figure 6. Plots of the predicted individual rate constants of the HNCO + C_3H_3 (R) reaction forming the C_4H_4NO (IS1–IS4) adducts and/or the H_2CCCH_2 + NCO (PR1)/$HCCCH_3$ + NCO (PR2) products in the 300–2000 K range and 76,000 Torr (Ar).

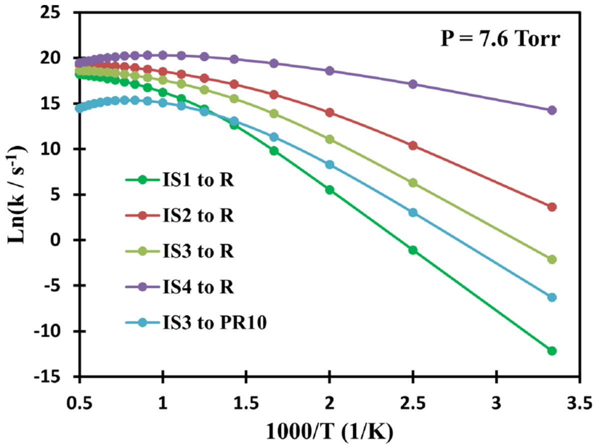

Figure 7. Plots of the predicted individual rate constants of the C_4H_4NO (IS1–IS4) → HNCO + C_3H_3 (R) reactions in the 300–2000 K range and 7.6 Torr (Ar).

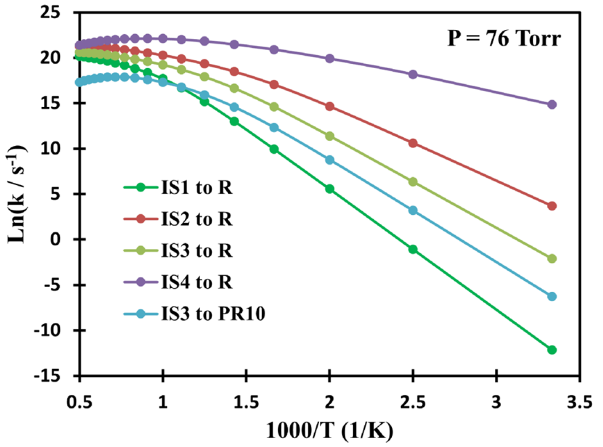

Figure 8. Plots of the predicted individual rate constants of the C_4H_4NO (IS1–IS4) → HNCO + C_3H_3 (R) reactions in the 300–2000 K range and 76 Torr (Ar).

are not affected by the changes in pressure because none of the intermediates is collisionally stabilized and are formed either directly from the reactants (HNCO + C_3H_3) of these two

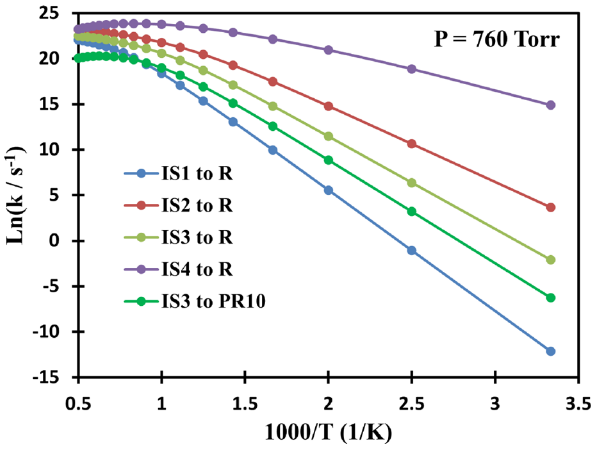

Figure 9. Plots of the predicted individual rate constants of the C_4H_4NO (IS1−IS4) → HNCO + C_3H_3 (R) reactions in the 300−2000 K range and 760 Torr (Ar).

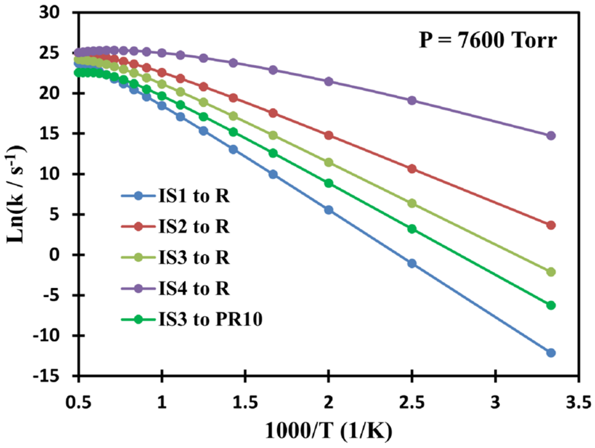

Figure 10. Plots of the predicted individual rate constants of the C_4H_4NO (IS1−IS4) → HNCO + C_3H_3 (R) reactions in the 300−2000 K range and 7600 Torr (Ar).

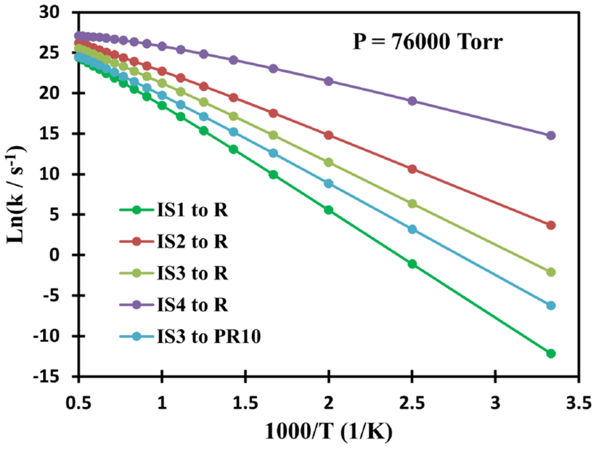

Figure 11. Plots of the predicted individual rate constants of the C_4H_4NO (IS1−IS4) → HNCO + C_3H_3 (R) reactions in the 300−2000 K range and 76,000 Torr (Ar).

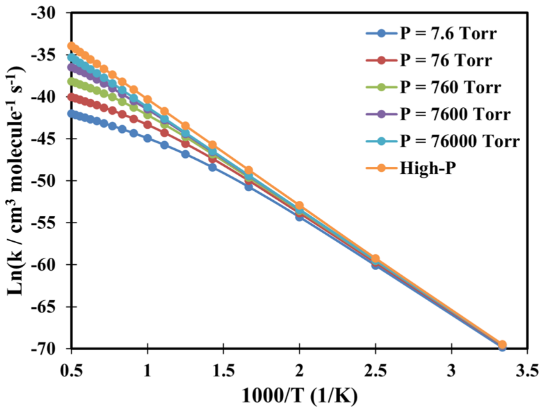

Figure 12. Plots of the predicted total rate constants of the bimolecular HNCO + C_3H_3 (R) → C_4H_4NO (IS1−IS4) reactions in the 300−2000 K temperature range and $P \geq 7.6$ Torr (Ar).

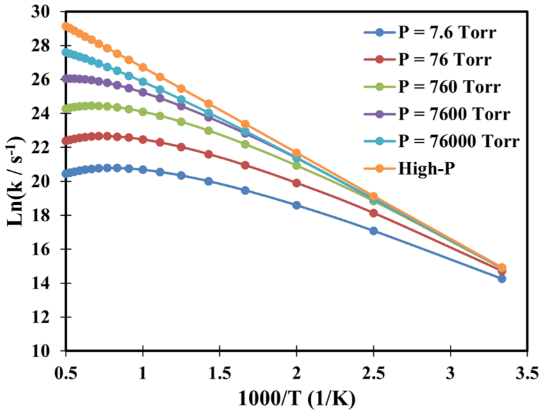

Figure 13. Plots of the predicted total rate constants of the unimolecular C_4H_4NO (IS1−IS4) → HNCO + C_3H_3 (R) reactions in the 300−2000 K temperature range and $P \geq 7.6$ Torr (Ar).

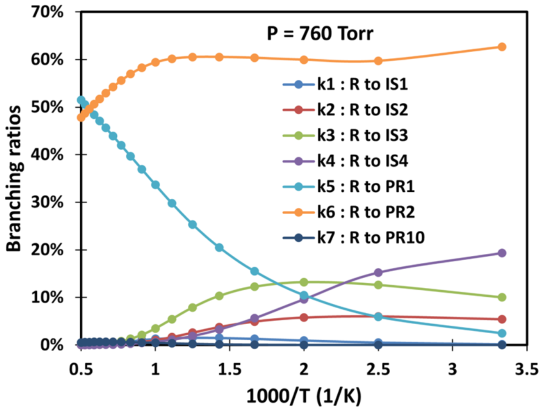

Figure 14. Branching ratios of the HNCO + C_3H_3 (R) → C_4H_4NO (IS1−IS4)/PR1/PR2/PR10 reactions in the 300−2000 K temperature range and P = 760 Torr (Ar).

pathways. Specifically, at P = 760 Torr, the k_5 pressure-independent rate coefficient ascends from the 4.41×10^{-32} cm^3 molecule^{-1} s^{-1} value at 300 K to the 9.00×10^{-15} cm^3 molecule^{-1} s^{-1} number at 2000 K, whereas the k_6 value jumps up to the 8.43×10^{-15} cm^3 molecule^{-1} s^{-1} number from the 1.14×10^{-30} cm^3 molecule^{-1} s^{-1} value in the 300−2000 K temperature range (see Table 2). At room temperature, it is easy to realize that the rate constant of the H-abstraction process, k_5: HNCO + C_3H_3 → H_2CCCH_2 + NCO (PR1), underestimates the k_6: HNCO + C_3H_3 → $HCCCH_3$ + NCO (PR2) rate coefficient by about 2 orders of magnitude. This is due to the fact that the energy barrier for the k_6 channel

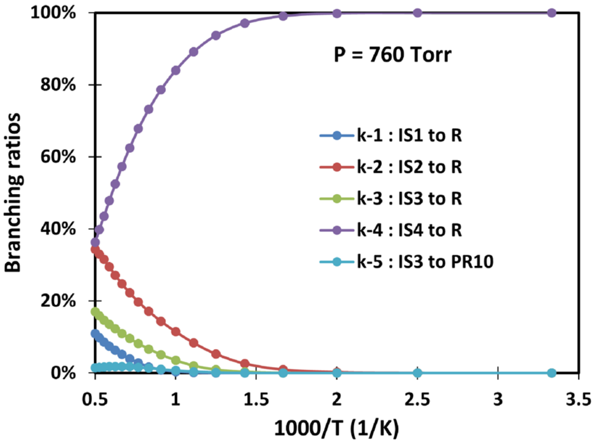

Figure 15. Branching ratios of the C_4H_4NO (IS1−IS4) → HNCO + C_3H_3 (R) and C_4H_4NO (IS3) → $HCCCH_2NH$ + CO (PR10) reactions in the 300−2000 K temperature range and P = 760 Torr (Ar).

(T0P2, 22.6 kcal/mol) is lower than that for the k_5 channel (T0P1, 24.8 kcal/mol), as shown in Figure 1. As the temperature increases (T > 900 K), however, the direct formation of the PR1 final product from the reactants becomes sufficient to compete with the immediate formation of the PR2 bimolecular product. This appears reasonable because high temperatures can help the reactants easily pass the T0P1 and T0P2 energy barriers. At elevated temperatures ($T \geq 1900$ K), the k_5 value shows signs of outperforming the k_6 number, for example, the 1900 K data of k_5 and k_6 have been recorded to be 5.65×10^{-15} and 5.39×10^{-15} cm^3 $molecule^{-1}$ s^{-1}, respectively; the branching ratios for the former are therefore higher than those for the latter (~51 and 52% vs ~49 and 48% at 1900 and 2000 K, respectively). Hence, it can be affirmatively said that the PR2 product formation is dominant to other processes in the considered temperature region (Figures 2−6), accounting for the ~50−63% branching ratio in the descending temperature range of 1800−300 K and 760 Torr pressure (Figure 14). This result is found to be in good agreement with the observation on the HNCO + C_3H_3 PES (cf. Figure 1) as discussed previously. Thus, it can again be asserted that PR2 is the major product of the HNCO + C_3H_3 → product reaction at any pressure and $T \leq 1800$ K, while the PR1 product holds the prevailing position at T > 1800 K.

Opposite to the HNCO + C_3H_3 (R) → PR1 and R → PR2 channels, the calculated R → PR10 rate constant is negligible under the given conditions. Its value, k_7, occupies the lowest place as compared to the calculated k_1−k_6 data (Figures 2−6). This is consistent because the R → PR10 channel has to overcome two high activation barriers (T0/3: 24 kcal/mol and T3P10: 26.5 kcal/mol, Figure 1). At 300 K and 760 Torr, for example, the k_7 value is approximately 7 orders of magnitude smaller than the k_6 number (5.89×10^{-37} vs 1.19×10^{-30} cm^3 $molecule^{-1}$ s^{-1}). Even though at a very high temperature, T = 2000 K, the k_7 rate constant still underestimates the k_6 value by nearly 2 orders of magnitude (see Table 2). The 760 Torr branching ratio for the PR10 formation does not exceed 0.7% under the 300−2000 K interval, cf. Figure 14, indicating that this product has minor contribution to the total products of the HNCO + C_3H_3 → products system. Another point should be noted that the lowest rate constant exhibits a negative pressure dependence. At 1000 K, for instance, the 7.6, 76, 760, 7600, and 76,000 Torr values of k_7 are predicted to be 1.04×10^{-19}, 7.97×10^{-20}, 3.47×10^{-20}, 7.11×10^{-21}, 8.35×10^{-22} cm^3 $molecule^{-1}$ s^{-1}, respectively.

For the HNCO + C_3H_3 → C_4H_4NO (IS1−IS4) addition processes, their bimolecular temperature-dependent rate constants, k_1−k_4, were found to display as a function of pressure, increasing with pressure, as shown in Figures 2−6. Their total temperature-dependent values are plotted in Figure 12, which reveals that these data strongly depend on pressure at high temperatures (T > 600 K); at low temperatures ($T \leq 600$ K), nevertheless, they seem to be nearly unaffected by pressure. Of the k_1−k_4 individual values, the first one in the low-temperature regime ($T \leq 500$ K) is much lower than those of the remaining values, for example, the 300 K & 760 Torr rate coefficient of k_1 is smaller than that of k_4 by about 2 orders of magnitude (3.26×10^{-33} vs 3.69×10^{-31} cm^3 $molecule^{-1}$ s^{-1}). This result is considered to be acceptable because the barrier height for the addition process of the R → IS1 channel is relatively high, accounting for over 26 kcal/mol compared to ~23 kcal/mol of the R → IS4 channel, as shown in Figure 1. The branching ratio for the formation of IS1 at 760 Torr pressure is less than 1.6% over the 300−2000 K temperature region (see Figure 14), showing that this adduct is hardly formed when C_3H_3 attacks HNCO. Except for the k_1 value, the three data k_2−k_3 can compete with the highest value of k_6 in the low-temperature domain ($T \leq 600$ K), for example, at P = 760 Torr, the 300−500 K calculated results for k_2, k_3, and k_4 have been obtained as 1.03×10^{-31} to 5.83×10^{-23}, 1.91×10^{-31}−1.45×10^{-22}, and 3.69×10^{-31} to 6.66×10^{-23} cm^3 $molecule^{-1}$ s^{-1} compared to the 1.19×10^{-30} to 7.16×10^{-22} cm^3 $molecule^{-1}$ s^{-1}. This is not unexpected as analyzed in the PES section because the k_2−k_4 activation barriers are similar to that of the k_6 channel, which is around 23−24 kcal/mol (Figure 1). The 760 Torr product yields of 4−6, 10−13, and 3−19%, in the reducing 700−300 K temperature interval, belong to the adducts IS2, IS3, and IS4, respectively, reflecting that these intermediates have a significant contribution to the total products of the bimolecular HNCO + C_3H_3 → products reaction. However, at higher temperatures (T > 1000 K) and any pressures, the contribution of all four addition channels forming IS1−IS4 can be negligible because their total product yield does not surpass 3%. Still, the total rate constant to form adducts and bimolecular products is very low, under 2.5×10^{-19} cm^3 $molecule^{-1}$ s^{-1} up to 800 K (any pressure), and hence the HNCO + C_3H_3 reaction in this temperature range can be ignored for all practical purposes. At higher temperatures, the total rate constant is still low and only exceeds 1.0×10^{-14} cm^3 $molecule^{-1}$ s^{-1} above 1900 K. Therefore, it can be concluded that in the high-temperature region, the bimolecular reaction can occur and predominantly produce PR1 and PR2.

The individual and total rate constants (in units of cm^3 $molecule^{-1}$ s^{-1}) for the bimolecular HNCO + C_3H_3 reaction in the temperature range of 300−2000 K at 760 Torr (Ar) can be expressed by the modified Arrhenius equation as follows

$$k_1(T) = 1.83T^{-4.21} \exp[(-30.87 \pm 0.63 \text{ kcal/mol})/RT)]$$

$$k_2(T) = 0.295T^{-4.18} \exp[(-27.66 \pm 0.21 \text{ kcal/mol})/RT)]$$

$$k_3(T) = 1.23 \times 10^3 T^{-5.13} \exp[(-29.14 \pm 0.39 \text{ kcal/mol})/RT)]$$

$$k_4(T) = 2.68 \times 10^{-2}T^{-4.01} \exp[(-25.98 \pm 0.01\ \text{kcal/mol})/RT)]$$

$$k_5(T) = 2.66 \times 10^{-22}T^{3.07} \exp[(-23.82 \pm 0.01\ \text{kcal/mol})/RT)]$$

$$k_6(T) = 4.7 \times 10^{-22}T^{2.91} \exp[(-21.69 \pm 0.01\ \text{kcal/mol})/RT)]$$

$$k_7(T) = 3.51 \times 10^{-10}T^{-0.87} \exp[(-33.78 \pm 0.01\ \text{kcal/mol})/RT)]$$

$$k_{\_\text{total}}(T) = 3.53 \times 10^{-23}T^{3.27} \exp[(-21.35 \pm 0.06\ \text{kcal/mol})/RT)]$$

So far, to the best of our knowledge, the rate constants for the reaction of the propargyl radical with isocyanic acid have not been investigated both experimentally and theoretically. Hence, there is no available data to compare the current calculated results. Nevertheless, it is informative to compare the activation barriers for the addition of HNCO to the C_3H_3 radical with those for the HCHO addition, which were reported in the 14−16 kcal/mol range[27] calculated at the CCSD(T)//B3LYP/6-311++G(3df,2p) level of theory. Obviously, the latter barriers are remarkably smaller than the former ones (23−26 kcal/mol). Moreover, the H-abstraction processes of the HNCO + C_3H_3 → C_3H_4 + NCO reaction are predicted to be significantly higher in activation energy compared to those of the HNCO + C_3H_3 → C_3H_4 + HCO channel[27] (∼23−25 kcal/mol vs ∼15−17 kcal/mol). As a consequence, the total second-order rate constants of the HNCO + C_3H_3 → product system are relatively larger than those of the HNCO + C_3H_3 → product reaction paths, which is 2.09×10^{-22} to 3.19×10^{-13} cm^3 molecule^{-1} s^{-1} for the former and 1.91×10^{-30} to 1.69×10^{-14} cm^3 molecule^{-1} s^{-1} for the latter in the 300−2000 K temperature interval. Thus, it can be said that HCHO is more reactive toward the C_3H_3 free radicals than HNCO.

For the decomposition processes, C_4H_4NO (IS1−IS4) → HNCO + C_3H_3 (k_{-1}−k_{-4}) and IS3 → PR10 (k_{-5}), their rate constants increase rapidly with temperature and pressure (Figures 7−11). At P < 76,000 Torr, however, it is worth bearing in mind that the k_{-4} and k_{-5} rate constants rise with T at a certain temperature regime and then slightly decreases when the temperature increases, for example, the 760 Torr values of k_{-4} and k_{-5} climb swiftly up to 2.29×10^{10} s^{-1} at 1200 K and 6.41×10^{8} s^{-1} at 1600 K from 2.96×10^{6} to 1.92×10^{-3} s^{-1} at 300 K, respectively; subsequently, the k_{-4} value reduces moderately in the $(6.65–2.83) \times 10^{8}$ s^{-1} range with $1100 \leq T \leq 2000$ K while the k_{-5} descends in the $(6.25–4.99) \times 10^{8}$ s^{-1} interval corresponding to $1700 \leq T \leq 2000$ K. Another point should be noted that at near room temperatures, the temperature-dependent rate coefficients are almost pressure-independent (Tables 3, S11−S14 and Figures 7−11, 13), for example, the 300 K rate constants of k_{-1} are 5.23×10^{-6}, 5.24×10^{-6}, 5.24×10^{-6}, 5.24×10^{-6}, and 5.24×10^{-6} s^{-1} at 7.6, 76, 760, 7600, and 7600 Torr, respectively. When the temperature gets higher, the k_{-1}−k_{-5} values become strongly dependent on pressure, as illustrated in Figure 13 for the calculated total rate constants at the high-pressure limit (high-P) and at finite pressures. From the PES (Figure 1), it is not difficult to realize that the reverse dissociation back to the reactants (HNCO + C_3H_3) of IS4 is most powerful with only ∼9 kcal/mol barrier height, followed by the decompositions of IS2 and IS3 whose activation barriers are ∼16 and ∼19 kcal/mol, respectively, whereas the IS1 → R channel is ranked at the bottom due to its high activation energy of nearly 26 kcal/mol. These results are completely consistent with the calculated rate-constant data, as shown in Figures 7−11. Particularly, in the P = 7.6−76,000 Torr range, the 300 K value of k_{-4} is about 5, 7, and 12 orders of magnitude larger than those of k_{-2}, k_{-3}, and k_{-1}, respectively. At higher temperatures, the deviations between them are getting smaller and smaller, for example, the 7.6 Torr rate coefficients of k_{-1}−k_{-4} are calculated to be 1.13×10^{7}, 1.11×10^{8}, 4.25×10^{7}, 6.67×10^{8} s^{-1} and 8.15×10^{7}, 2.31×10^{8}, 1.25×10^{8}, 2.83×10^{8} s^{-1} at 1000 and 2000 K, respectively. A similar trend is also recorded at the higher pressures (Figures 8−11). These computed results indicate that the IS4 → C_3H_3 + HNCO decomposition is the major channel of the C_4H_4NO decomposition in the considered temperature region and any pressure. The branching ratio for this channel accounts for 36−100% in the reducing 2000−300 K temperature range and 760 Torr, followed by the decompositions of IS2 and IS3 to the reactants with the yields of 0−34 and 0−17%, respectively, under the same conditions. At an elevated temperature regime (T > 2000 K), all of the four IS1−IS4 → HNCO + C_3H_3 reverse reactions can become strongly competitive with each other. For the formation of PR10, the barrier on the IS3 → PR10 pathway for dissociation of IS3 is relatively higher than that in the reverse direction back to the reactants, and hence this channel is not competitive until the temperature and the pressure become high enough (T > 2000 K and P > 76,000 Torr). The 760 Torr branching ratio of the PR10 product was calculated to be less than 1% over the 300−2000 K temperature interval (Figure 15). This value can increase to well over 4% at T = 2000 K and P = 76,000 Torr. However, it is still too small to compete with the ∼96% total product yield of the HNCO + C_3H_3 formation under the same conditions. Therefore, in the considered T- and P-ranges, the C_4H_4NO decomposition reaction flux goes nearly exclusively to the HNCO + C_3H_3, while the PR10 product can be ignored due to its low branching ratio as indicated.

The predicted total rate constants for the C_4H_4NO → product decomposition were fitted to the modified Arrhenius equation, yielding the expression of k(300−2000 K, 760 Torr) = $1.13 \times 10^{25}T^{-4.02} \exp(-11.77 \pm 0.16\ \text{kcal/mol/RT})$ s^{-1}.

5. CONCLUSIONS

The detailed mechanism and kinetics of the formation and decomposition of C_4H_4NO, an important species in the atmosphere and combustion chemistry, were intensively investigated utilizing the accurate electronic structure calculations at the CCSD(T)/CBS(T,Q,5)//B3LYP/6-311++G(3df,2p) level and the rigorous ME/RRKM kinetic model. The constructed PES revealed that the HNCO + C_3H_3 reaction can proceed via two mechanism reactions, namely, the N/C/O addition and direct H-abstraction channels to possibly yield the final products, H_3CCCH + NCO (PR1), H_2CCCH_2 + NCO (PR2), and $HCCCH_2NH$ + CO (PR10). For H-abstractions, the reaction channels go through the T0P1 and T0P2 activation barriers lying at 24.8 and 22.6 kcal/mol, respectively, above the reactants, whereas the addition processes have to overcome higher barriers of 23.4−26.3 kcal/mol. Furthermore, the reverse decomposition processes of C_4H_4NO back to the reactants outweigh the forward dissociations of it to products.

The calculated rate constants and product branching ratios for the HNCO + C_3H_3 reaction show that the reaction may be significant only in the high-temperature region, at the temperature above 1500 K under any pressure. At $T \leq 1800$ K, the H-abstraction process leading to the H_3CCCH + NCO product via the barrier of 22.6 kcal/mol is the prevailing reaction channel with the 760 Torr branching ratio of ∼50−53% in the descending 1800−1500 K temperature range, while the other H-abstraction forming the H_2CCCH_2 + NCO product via the 24.8 kcal/mol activation energy is dominant at $T > 1800$ K with the 760 Torr yield above 50%. The rate constants of the HNCO + C_3H_3 reaction resulting in the two bimolecular products PR1 and PR2 are pressure-independent and increase with temperature, whereas those of the HNCO + $C_3H_3 \rightarrow C_4H_4NO$ and HNCO + $C_3H_3 \rightarrow HCCCH_2NH + CO$ reactions are found to be pressure-dependent. The calculated total rate constants for the HNCO + C_3H_3 bimolecular reaction in the T = 300−2000 K temperature range and P = 760 Torr have been fitted to the modified Arrhenius equation leading to $k_{\text{total}}(T) = 3.53 \times 10^{-23}T^{3.27} \exp[(-21.35 \pm 0.06\ \text{kcal/mol})/RT]\ \text{cm}^3\ \text{molecule}^{-1}\ \text{s}^{-1}$. This total rate constant is estimated to be significantly smaller than the total rate coefficient of HCHO + C_3H_3 → products, which is about 8 orders of magnitude smaller calculated at 300 K. It can therefore conclude that HCHO is more reactive toward the C_3H_3 free radicals than HNCO.

For the decomposition processes, C_4H_4NO (IS1−IS4) → HNCO + C_3H_3 and IS3 → PR10, their rate constants depend significantly on temperatures and pressures. Of which, the IS4 → HNCO + C_3H_3 channel was recorded to be the most favorable reaction path with only ∼9 kcal/mol barrier height. The 760 Torr branching ratio for this channel accounts for 100% at 300 K and then gradually reduces to 36% at 2000 K. The predicted total rate constants for the decomposition reaction C_4H_4NO → products were fitted to the modified Arrhenius equation, yielding the expression of $k(300{-}2000\ \text{K}, 760\ \text{Torr}) = 1.13 \times 10^{25}T^{-4.02} \exp(-11.77 \pm 0.16\ \text{kcal/mol}/RT)\ \text{s}^{-1}$. It is recommended that the given detailed kinetic mechanism including the computed rate constants and thermodynamic data of the species involved should be accounted for the modeling/simulation of both atmospheric and combustion applications (i.e., T = 300−2000 K and P = 7.6−76,000 Torr).

■ ASSOCIATED CONTENT

Supporting Information

The Supporting Information is available free of charge at https://pubs.acs.org/doi/10.1021/acsomega.1c05063.

> Theoretical prediction of single-point energies and ZPE for reactants, intermediates, TSs, and products of the C_3H_3 + HNCO reaction at different levels; Gibbs free energies (ΔG) in kcal/mol and entropies (ΔS) in cal/mol/K of the reaction channels in the C_3H_3 + HNCO system at the CCSD(T)/CBS//B3LYP/6-311++G-(3df,2p) level; frequencies of reactants, intermediates, TSs, and products of the C_3H_3 + HNCO reaction using B3LYP/6-311++G(3df,2p); optimized coordinates of reactants, intermediates, TSs, and products of the C_3H_3 + HNCO reaction at the B3LYP/6-311++G(3df,2p) level of theory; relative energies of several main TSs of the C_3H_3 + HNCO system in different methods; spin contamination $\langle S^2 \rangle$ at the B3LYP/6-311++G(3df,2p) level and the T1 diagnostic at the CCSD(T)/aug-cc-pVTZ level; the bimolecular k_1−k_7 rate constants (in units of $\text{cm}^3\ \text{molecule}^{-1}\ \text{s}^{-1}$) of the C_3H_3 + HNCO reaction calculated at T = 300−2000 K and P = 7.6−76,000 Torr (Ar); k_{-1}−k_{-5} unimolecular rate constants (in units of s^{-1}) of the C_4H_4NO (IS1−IS4) → C_3H_3 + HNCO and C_4H_4NO (IS3) → $HCCCH_2NH$ + CO (PR10) decomposition reactions calculated at T = 300−2000 K and P = 7.6−76,000 Torr (Ar); hindrance potentials for the species involved in the C_3H_3 + HNCO reaction, calculated at the B3LYP/6-311++G(3df,2p) level of theory; geometries of the reactants, intermediate states, TSs, and products optimized at the B3LYP/6-311++G(3df,2p) level; and IRC scan results for the T0P1 and T0P2 TSs implemented at the B3LYP/6-311++G(3df,2p) level of theory (PDF)

■ AUTHOR INFORMATION

Corresponding Author

Tien Van Pham − *School of Chemical Engineering, Hanoi University of Science and Technology, Hanoi 100000, Vietnam;* orcid.org/0000-0002-2067-9028;
Email: tien.phamvan@hust.edu.vn

Author

Anh Van Tran − *School of Chemical Engineering, Hanoi University of Science and Technology, Hanoi 100000, Vietnam*

Complete contact information is available at:
https://pubs.acs.org/10.1021/acsomega.1c05063

Notes

The authors declare no competing financial interest.

■ ACKNOWLEDGMENTS

This research is funded by Hanoi University of Science and Technology (HUST) under grant number T2021-PC-046. We also acknowledge the National Center for High-Performing Computers in Taiwan for the use of its facility.

■ REFERENCES

(1) Liebig, J.; Wöhler, F. Untersuchungen über die Cyansäure. *Ann. Phys.* **1830**, *96*, 369−400.

(2) Roberts, J. M.; Veres, P. R.; Cochran, A. K.; Warneke, C.; Burling, I. R.; Yokelson, R. J.; Lerner, B.; Gilman, J. B.; Kuster, W. C.; Fall, R.; de Gouw, J. Isocyanic acid in the atmosphere and its possible link to smoke-related health effects. *Proc. Natl. Acad. Sci. U.S.A.* **2011**, *108*, 8966−8971.

(3) Wentzell, J. J. B.; Liggio, J.; Li, S.-M.; Vlasenko, A.; Staebler, R.; Lu, G.; Poitras, M.-J.; Chan, T.; Brook, J. R. Measurements of Gas phase Acids in Diesel Exhaust: A Relevant Source of HNCO? *Environ. Sci. Technol.* **2013**, *47*, 7663−7671.

(4) Zabardasti, A.; Kakanejadifard, A.; Kikhaei, M.; Solimannejad, M. Theoretical studies and topological analysis of the electron density of clusters of O_3 with HNCO and HCNO. *J. Mol. Struct.: THEOCHEM* **2010**, *961*, 1−5.

(5) Roberts, J. M.; Veres, P.; Warneke, C.; Neuman, J. A.; Washenfelder, R. A.; Brown, S. S.; Baasandorj, M.; Burkholder, J. B.; Burling, I. R.; Johnson, T. J.; Yokelson, R. J.; de Gouw, J. Measurement of HONO, HNCO, and other inorganic acids by

negative-ion proton-transfer chemical-ionization mass spectrometry (NI-PT-CIMS): application to biomass burning emissions. *Atmos. Meas. Tech.* **2010**, *3*, 981−990.

(6) Wang, Z.; Nicholls, S. J.; Rodriguez, E. R.; Kummu, O.; Hörkkö, S.; Barnard, J.; Reynolds, W. F.; Topol, E. J.; DiDonato, J. A.; Hazen, S. L. Protein carbamylation links inflammation, smoking, uremia and atherogenesis. *Nat. Med.* **2007**, *13*, 1176−1184.

(7) Leslie, M. D.; Ridoli, M.; Murphy, J. G.; Borduas-Dedekind, N. Isocyanic acid (HNCO) and its fate in the atmosphere: a review. *Environ. Sci.: Processes Impacts* **2019**, *21*, 793−808.

(8) Veres, P.; Roberts, J. M.; Burling, I. R.; Warneke, C.; de Gouw, J.; Yokelson, R. J. Measurements of gas-phase inorganic and organic acids from biomass fires by negative-ion proton-transfer chemical-ionization mass spectrometry. *J. Geophys. Res.* **2010**, *115*, D23302.

(9) Nelson, P. F.; Li, C.-Z.; Ledesma, E. Formation of HNCO from the rapid pyrolysis of coals. *Energy Fuels* **1996**, *10*, 264−265.

(10) Barnes, I.; Solignac, G.; Mellouki, A.; Becker, K. H. Aspects of the atmospheric chemistry of amides. *Eur. J. Chem.* **2010**, *11*, 3844−3857.

(11) Heeb, N. V.; Zimmerli, Y.; Czerwinski, J.; Schmid, P.; Zennegg, M.; Haag, R.; Seiler, C.; Wichser, A.; Ulrich, A.; Honegger, P.; Zeyer, K.; Emmenegger, L.; Mosimann, T.; Kasper, M.; Mayer, A. Reactive nitrogen compounds (RNCs) in exhaust of advanced PM−NO_x abatement technologies for future diesel applications. *Atmos. Environ.* **2011**, *45*, 3203−3209.

(12) Brady, J. M.; Crisp, T. A.; Collier, S.; Kuwayama, T.; Forestieri, S. D.; Perraud, V.; Zhang, Q.; Kleeman, M. J.; Cappa, C. D.; Bertram, T. H. Real-Time Emission Factor Measurements of Isocyanic Acid from Light Duty Gasoline Vehicles. *Environ. Sci. Technol.* **2014**, *48*, 11405−11412.

(13) Baker, R. R.; Bishop, L. J. The pyrolysis of tobacco ingredients. *J. Anal. Appl. Pyrolysis* **2004**, *71*, 223−311.

(14) Borduas, N.; Murphy, J. G.; Wang, C.; da Silva, G.; Abbatt, J. P. D. Gas Phase Oxidation of Nicotine by OH Radicals: Kinetics, Mechanisms, and Formation of HNCO. *Environ. Sci. Technol. Lett.* **2016**, *3*, 327−331.

(15) Blomqvist, P.; Hertzberg, T.; Dalene, M.; Skarping, G. Isocyanates, aminoisocyanates and amines from fires – a screening of common materials found in buildings. *Fire Mater.* **2003**, *27*, 275−294.

(16) Jankowski, M. J.; Olsen, R.; Nielsen, C. J.; Thomassen, Y.; Molander, P. The applicability of proton transfer reaction-mass spectrometry (PTR-MS) for determination of isocyanic acid (ICA) in work room atmospheres. *Environ. Sci.: Processes Impacts* **2014**, *16*, 2423−2431.

(17) Baulch, D. L.; Bowman, C. T.; Cobos, C. J.; Cox, R. A.; Just, T.; Kerr, J. A.; Pilling, M. J.; Stocker, D.; Troe, J.; Tsang, W.; Walker, R. W.; Warnatz, J. Evaluated Kinetic Data for Combustion Modeling: Supplement II. *J. Phys. Chem. Ref. Data* **2005**, *34*, 757.

(18) Mertens, J. D.; Chang, A. Y.; Hanson, R. K.; Bowman, C. T. A Shock-Tube Study of Reactions of Atomic Oxygen with Isocyanic Acid. *Int. J. Chem. Kinet.* **1992**, *24*, 279−295.

(19) Tsang, W. Chemical Kinetic Data Base for Propellant Combustion. II. Reactions Involving CN, NCO, and HNCO. *J. Phys. Chem. Ref. Data* **1992**, *21*, 753.

(20) Tully, F. P.; Perry, R. A.; Thorne, L. R.; Allendorf, M. D. Free-radical oxidation of isocyanic acid. *Symp. (Int.) Combust., [Proc.]* **1989**, *22*, 1101−1106.

(21) Wooldridge, M. S.; Hanson, R. K.; Bowman, C. T. A shock tube study of CO+OH→CO_2+H and HNCO+OH→productsvia simultaneous laser adsorption measurements of OH and CO2. *Int. J. Chem. Kinet.* **1996**, *28*, 361−372.

(22) Sengupta, D.; Nguyen, M. T. Mechanism of NH_2+CO_2 formation in OH+HNCOreaction :Rate constant evaluation via ab initio calculations and statistical theory. *J. Chem. Phys.* **1997**, *106*, 9703−9707.

(23) Rosanka, S.; Vu, G. H. T.; Nguyen, H. M. T.; Pham, T. V.; Javed, U.; Taraborrelli, D.; Vereecken, L. Atmospheric chemical loss processes of isocyanic acid (HNCO): a combined theoretical kinetic and global modelling study. *Atmos. Chem. Phys.* **2020**, *20*, 6671−6686.

(24) Miller, J. A.; Pilling, M. J.; Troe, J. Unravelling combustion mechanisms through a quantitative understanding of elementary reactions. *Proc. Combust. Inst.* **2005**, *30*, 43−88.

(25) Tian, W. Q.; Wang, Y. A. Mechanisms of Staudinger Reactions within Density Functional Theory. *J. Org. Chem.* **2004**, *69*, 4299−4308.

(26) Lee, I.; Kyung Kim, C.; Lee, B.-S.; Ha, T.-K. Theoretical studies on the reaction of phosphoranes with anions. *J. Mol. Struct.* **1993**, *279*, 191−205.

(27) Pham, T. V. Theoretical Investigation on Mechanism, Thermochemistry, and Kinetics of the Gas-phase Reaction of 2-Propargyl Radical with Formaldehyde. *Chem. Res. Chin. Univ.* **2019**, *35*, 884−891.

(28) Pham, T. V.; Tue Trang, H. T. Combination Reactions of Propargyl Radical with Hydroxyl Radical and the Isomerization and Dissociation of trans-Propenal. *J. Phys. Chem. A* **2020**, *124*, 6144−6157.

(29) Pham, T. V.; Trang, H. T. T.; Ngo, C. T.; Nguyen, H. M. T. A quantum chemical study of the mechanisms and kinetics of the reaction between propargyl (C_3H_3) and methyl (CH_3) radicals. *Chem. Phys. Lett.* **2021**, *762*, 138126.

(30) Nguyen, H. M. T.; Pham, T. V.; Van Hoang, H.; Hoan, P. T.; Cuong, N. T. Mechanism and kinetics of the reaction of the 2-propargyl radical with ammonia. *Int. J. Chem. Kinet.* **2020**, *52*, 84−91.

(31) Becke, A. D. Density functional thermochemistry. III. The role of exact exchange. *J. Chem. Phys.* **1993**, *98*, 5648−5652.

(32) Becke, A. D. Density-functional exchange-energy approximation with correct asymptotic-behavior. *Phys. Rev. A: At., Mol., Opt. Phys.* **1988**, *38*, 3098−3100.

(33) Lee, C.; Yang, W.; Parr, R. G. Development of the Colle-Salvetti correlation-energy formula into a functional of the electron density. *Phys. Rev. B: Condens. Matter Mater. Phys.* **1988**, *37*, 785−789.

(34) Krishnan, R.; Binkley, J. S.; Seeger, R.; Pople, J. A. Self-consistent molecular orbital methods. XX. A basis set for correlated wave functions. *J. Chem. Phys.* **1980**, *72*, 650.

(35) Gonzalez, C.; Schlegel, H. B. An improved algorithm for reaction path following. *J. Chem. Phys.* **1989**, *90*, 2154−2161.

(36) Gonzalez, C.; Schlegel, H. B. Reaction path following in mass-weighted internal coordinates. *J. Chem. Phys.* **1990**, *94*, 5523−5527.

(37) Chen, H.-T.; Pham, T. V.; Lin, M. C. Computational study on the mechanisms and rate constants for the $O(^3P,^1D)$ + OCS reactions. *J. Phys. Chem. A* **2019**, *123*, 8358−8364.

(38) Pham, T. V.; Trang, H. T. T.; Huyen, T. L.; Nguyen, T. N. Theoretical study of the kinetics of the gas-phase reaction between phenyl and amino radicals. *Omega* **2020**, *5*, 1277−1286.

(39) Pham, T. V.; Tsay, T. J.; Lin, M. C. Thermal decomposition of N_2O near 900 K studied by FTIR spectrometry: Comparison of experimental and theoretical $O(^3P)$ formation kinetics. *Int. J. Chem. Kinet.* **2020**, *52*, 632−644.

(40) Lanfri, L.; Wang, Y.-L.; Pham, T. V.; Nguyen, N. T.; Paci, M. B.; Lin, M. C.; Lee, Y.-P. Infrared Emission from Photodissociation of Methyl Formate [$HC(O)OCH_3$] at 248 and 193 nm: Absence of Roaming Signature. *J. Phys. Chem. A* **2019**, *123*, 6130−6143.

(41) Pham, T. V.; Nguyen, H. M. T.; Lin, M. C. On the hypergolicity of trimethyl aluminum in air. *Comput. Theor. Chem.* **2020**, *1173*, 112668.

(42) Huyen, T. L.; Pham, T. V.; Nguyen, M. T.; Lin, M. C. A model study on the mechanism and kinetics for reactions of the hydrated electron with H_3O^+ and NH_4^+ ions. *Chem. Phys. Lett.* **2019**, *731*, 136604.

(43) Pham, T. V.; Lin, M. C. Ab Initio Quantum-Chemical and Kinetic Studies of the $O(^1D)$ + $N_2(X^1\Sigma_g^+)$ Spin-Forbidden Quenching Process. *Chem. Phys. Lett.* **2021**, *780*, 138955.

(44) Raghavachari, K.; Trucks, G. W.; Pople, J. A.; Head-Gordon, M. A fifth-order perturbation comparison of electron correlation theories. *Chem. Phys. Lett.* **1989**, *157*, 479−483.

(45) Dunning, T. H., Jr. Gaussian basis sets for use in correlated molecular calculations. I. The atoms boron through neon and hydrogen. *J. Chem. Phys.* **1989**, *90*, 1007−1023.

(46) Kendall, R. A.; Dunning, T. H., Jr.; Harrison, R. J. Electron affinities of the first-row atoms revisited. Systematic basis sets and wave functions. *J. Chem. Phys.* **1992**, *96*, 6796−6806.

(47) Woon, D. E.; Dunning, T. H., Jr. Gaussian basis sets for use in correlated molecular calculations. III. The atoms aluminum through argon. *J. Chem. Phys.* **1993**, *98*, 1358−1371.

(48) Van Pham, T.; Nguyen, T. N.; Trang, H. T. T. Computational Investigation on the Formation and Decomposition Reactions of the C_4H_3O Compound. *Omega* **2021**, *6*, 17965−17976.

(49) Chen, J. L.; Sun, T.; Wang, Y. B.; Wang, W. Toward a less costly but accurate calculation of the CCSD(T)/CBS noncovalent interaction energy. *J. Comput. Chem.* **2020**, *41*, 1252−1260.

(50) Pham, T. V.; Tue Trang, H. T. Theoretical Investigation of the Mechanisms and Kinetics of the Bimolecular and Unimolecular Reactions Involving in the C_4H_6 Species. *J. Phys. Chem. A* **2021**, *125*, 585−596.

(51) Pham, T. V.; Trang, H. T. T. A theoretical study on mechanism and kinetics of the C_2H_3 + C_2H_3 recombination and the isomerization and dissociation of butadiene. *Chem. Phys.* **2021**, *548*, 111217.

(52) Lee, T. J.; Taylor, P. R. A diagnostic for determining the quality of single-reference electron correlation methods. *Int. J. Quantum Chem.* **1989**, *36*, 199−207.

(53) Jayatilaka, D.; Lee, T. J. Open-shell coupled-cluster theory. *J. Chem. Phys.* **1993**, *98*, 9734−9747.

(54) Frisch, M. J.; Trucks, G. W.; Schlegel, H. B.; Scuseria, G. E.; Robb, M. A.; Cheeseman, J. R.; Scalmani, G.; Barone, V.; Petersson, G. A.; Nakatsuji, H.; Li, X.; Caricato, M.; Marenich, A.; Bloino, J.; Janesko, B. G.; Gomperts, R.; Mennucci, B.; Hratchian, H. P.; Ortiz, J. V.; Izmaylov, A. F.; Sonnenberg, J. L.; Williams-Young, D.; Ding, F.; Lipparini, F.; Egidi, F.; Goings, J.; Peng, B.; Petrone, A.; Henderson, T.; Ranasinghe, D.; Zakrzewski, V. G.; Gao, J.; Rega, N.; Zheng, G.; Liang, W.; Hada, M.; Ehara, M.; Toyota, K.; Fukuda, R.; Hasegawa, J.; Ishida, M.; Nakajima, T.; Honda, Y.; Kitao, O.; Nakai, H.; Vreven, T.; Throssell, K.; Montgomery, J. A.; Peralta, J. E.; Ogliaro, F.; Bearpark, M.; Heyd, J. J.; Brothers, E.; Kudin, K. N.; Staroverov, V. N.; Keith, T.; Kobayashi, R.; Normand, J.; Raghavachari, K.; Rendell, A.; Burant, J. C.; Iyengar, S. S.; Tomasi, J.; Cossi, M.; Millam, J. M.; Klene, M.; Adamo, C.; Cammi, R.; Ochterski, J. W.; Martin, R. L.; Morokuma, K.; Farkas, O.; Foresman, J. B.; Fox, D. J. *Gaussian 16*; Gaussian, Inc.: Wallingford CT, USA, 2016.

(55) Eyring, H. The Activated Complex in Chemical Reactions. *J. Chem. Phys.* **1935**, *3*, 107−115.

(56) Evans, M. G.; Polanyi, M. Some applications of the transition state method to the calculation of reaction velocities, especially in solution. *Trans. Faraday Soc.* **1935**, *31*, 875−894.

(57) Holbrook, K. A.; Pilling, M. J.; Robertson, S. H. *Unimolecular Reactions*; Wiley, 1996.

(58) Wardlaw, D. M.; Marcus, R. A. RRKM reaction rate theory for transition states of any looseness. *Chem. Phys. Lett.* **1984**, *110*, 230−234.

(59) Klippenstein, S. J.; Marcus, R. A. Unimolecular Reaction Rate Theory for Highly Flexible Transition States. 2. Conventional Coordinate Formulas for the Various Possible Fragment Combinations. Miscellaneous Topics. *J. Phys. Chem.* **1988**, *92*, 5412−5417.

(60) Mokrushin, V.; Bedanov, V.; Tsang, W.; Zachariah, M.; Knyazev, V. *ChemRate*, version 1.5.8; NIST: Gaithersburg, MD, 2009.

(61) Glowacki, D. R.; Liang, C.-H.; Morley, C.; Pilling, M. J.; Robertson, S. H. MESMER an open-source master equation solver for multi-energy well reactions. *J. Phys. Chem. A* **2012**, *116*, 9545−9560.

(62) Eckart, C. The Penetration of a Potential Barrier by Electrons. *Phys. Rev.* **1930**, *35*, 1303−1309.

(63) Stein, S. E.; Rabinovitch, B. S. Accurate evaluation of internal energy level sums and densities including anharmonic oscillators and hindered rotors. *J. Chem. Phys.* **1973**, *58*, 2438−2445.

(64) Beyer, T.; Swinehart, D. F. Number of multiply-restricted partitions. *Commun. ACM* **1973**, *16*, 379.

(65) Hippler, H.; Troe, J.; Wendelken, H. J. Collisional deactivation of vibrationally highly excited polyatomic molecules. II. Direct observations for excited toluene. *J. Chem. Phys.* **1983**, *78*, 6709−6717.

(66) Miller, J. A.; Klippenstein, S. J. The H+C_2H_2 (+M) ↔ C_2H_3 (+M) and H+C_2H_2 (+M) ↔ C_2H_5 (+M) reactions: Electronic structure, variational transition-state theory, and solutions to a two-dimensional master equation. *Phys. Chem. Chem. Phys.* **2004**, *6*, 1192−1202.

(67) Ruscic, B.; Pinzon, R. E.; Laszewski, G. V.; Kodeboyina, D.; Burcat, A.; Leahy, D.; Montoy, D.; Wagner, A. F. Active Thermochemical Tables: thermochemistry for the 21st century. *J. Phys.: Conf. Ser.* **2005**, *16*, 561−570.

(68) Ruscic, B.; Pinzon, R. E.; Morton, M. L.; Srinivasan, N. K.; Su, M.-C.; Sutherland, J. W.; Michael, J. V. Active Thermochemical Tables:Accurate Enthalpy of Formation of Hydroperoxyl Radical ,HO2. *J. Phys. Chem. A* **2006**, *110*, 6592−6601.